tron ambient dose equivalents per the treatment absorbed dose at the center of the range-modulated region $H^*(10)/D_t$ as measured with the rem meter WENDI-II (Ref. 46) are shown.[6] [WENDI-II used in the previous study was calibrated by using an ^{241}Am–Be neutron source and then could directly output $H^*(10)$.]

The H/D_t values obtained in this study were two to three times higher than those by Wroe *et al.*[20] This difference should be attributed to the facility dependency according to our previous study. However, since the experimental data are too scarce to confirm this, more experimental data at different facilities are needed. Also, it was found that the neutron ambient dose equivalent obtained with WENDI-II in the previous paper[6] provides a conservative dose estimation compared to the dose equivalent in the phantom. This result shows that measuring the undesired dose with a rem meter such as WENDI-II is good for the first estimation because the measurement with a rem meter is convenient and easy; however, the dose measurement in a phantom is needed for accurate risk assessment of secondary cancer.

Q_D values of this study were in good agreement with those of Wroe *et al.*[20] except for our 5.2 cm WED. Since the contribution of secondary neutrons produced in the beam-shaping devices was higher at 5.2 cm WED (d=5 cm) as written above, we expect that this difference is due to the facility dependency. However, it should be true that Q_D is higher as the position is closer to the phantom surface because the contribution of secondary neutrons produced in the beam-shaping devices with a high quality factor is higher. As the position became closer to the field edge (within ~20 cm from the field edge), Q_D decreased by 2 according to Wroe *et al.*[20] This is due to the scatter of incident protons as fragmental protons in the carbon beam. Also, Wroe *et al.*[20] mentioned that Q_D is relatively constant with a value of 5–6 after the distal edge. When our data were combined with that from Wroe *et al.*,[20] the following conclusions could be made: (1) At a position close to the field edge within ~20 cm from the field edge, Q_D is 2–5. (2) At a position close to the beam-shaping devices, Q_D is 7–8. There is a possibility that this value varies depending on the facility. (3) At other positions, Q_D is 5–6, which is here defined as the equilibrium Q_D. The equilibrium Q_D should depend on the energy of the incident proton beam as shown in the carbon beam. The conclusion for Q_D can be applied to the incident carbon beam. In carbon radiotherapy, Q_D is 2–4 within ~50 cm from the field edge and the equilibrium Q_D is 4–5.

V. CONCLUSIONS

We experimentally obtained absorbed doses, dose-averaged quality factors, and dose equivalents in water phantom outside of the irradiation field in passive carbon-ion and proton radiotherapies with TEPC. These data are very useful for estimating the risk of secondary cancer in patients receiving passive radiotherapies and for verifying Monte Carlo calculations, which can provide more detailed dose distribution. The comparison between carbon-ion and proton radiotherapies was done with approximately the same parameter settings of beam-shaping devices and exactly the same experimental setup. Assuming a prostate cancer treatment in which the total prescribed dose was 66 GyE for the 400 MeV/u carbon beam and 74 GyE for the 235 MeV proton beam, the total secondary exposure doses per treatment were comparable to or less than those in 3D-CRT and IMRT at all positions. In particular, as the position became closer to the field edge, the total dose equivalents in carbon-ion and proton radiotherapies were obviously less than those in 3D-CRT and IMRT. It was also found that the distributions and values of D/D_t, H/D_t, and Q_D differed for carbon-ion and proton radiotherapies. Combining the published data for proton beam and the results obtained in this study, the distribution of Q_D in water phantom was shown for a proton beam.

We are now working on verifying the Monte Carlo calculation of the dose distribution in water phantom with the experimental data from this study. We then plan to assess the organ-specific dose in an anthropomorphic phantom, which is essential to the risk assessment of the secondary cancer risk. Our final goal is to develop a system for assessing the secondary exposure dose of any patient receiving passive carbon-ion or proton radiotherapy.

[a]Electronic mail: yonai@nirs.go.jp

[1]H. Tsujii *et al.*, "Overview of clinical experiences on carbon ion radiotherapy at NIRS," Radiother. Oncol. **73**, S41–S49 (2004).
[2]H. H. Tsujii, J. Mizoe, T. Kamada, M. Baba, H. Tsuji, S. Kato, H. Kato, S. Yamada, S. Yasuda, T. Ohno, T. Yanagi, R. Imai, K. Kagei, H. Kato, R. Hara, A. Hasegawa, M. Nakajima, N. Sugane, N. Tamaki, R. Takagi, S. Kandatsu, K. Yoshikawa, R. Kishimoto, and T. Miyamoto, "Clinical results of carbon ion radiotherapy at NIRS," J. Radiat. Res. (Tokyo) **48**, A1–A13 (2007).
[3]C. Z. Jarlskog and H. Paganetti, "Risk of developing second cancer from neutron dose in proton therapy as function of field characteristics, organ and patient age," Int. J. Radiat. Oncol., Biol., Phys. **72**(1), 228–235 (2008).
[4]E. Hall, "Intensity-modulated radiation therapy, protons, and the risk of second cancers," Int. J. Radiat. Oncol., Biol., Phys. **65**(1), 1–7 (2006).
[5]U. Schneider, A. Lomax, and N. Lombriser, "Comparative risk assessment of secondary cancer incidence after treatment of Hodgkin's disease with photon and proton radiation," Radiat. Res. **154**(4), 382–388 (2000).
[6]S. Yonai, N. Matsufuji, T. Kanai, Y. Matsui, K. Matsusita, H. Yamashita, M. Numano, T. Sakae, T. Terunuma, T. Nishio, R. Kohno, and T. Akagi, "Measurement of neutron ambient dose equivalent in passive carbon-ion and proton radiotherapies," Med. Phys. **35**(11), 4782–4792 (2008).
[7]U. Schneider, S. Agosteo, E. Pedroni, and J. Besserer, "Secondary neutron dose during proton therapy using spot scanning," Int. J. Radiat. Oncol., Biol., Phys. **53**, 244–251 (2002).
[8]H. Iwase, K. Gunzert-Marx, E. Haettner, D. Schardt, F. Gutermuth, M. Kraemer, and G. Kraft, "Experimental and theoretical study of the neutron dose produced by carbon ion therapy beams," Radiat. Prot. Dosim. **126**(1–4), 615–618 (2007).
[9]K. Gunzert-Marx, D. Schardt, and R. S. Simon, "The fast neutron component in treatment irradiations with 12C beam," Radiother. Oncol. **73**, S92–S95 (2004).
[10]K. Gunzert-Marx, D. Schardt, and R. S. Simon, "Fast neutrons produced by nuclear fragmentation in treatment irradiations with 12C beam," Radiat. Prot. Dosim. **110**(1–4), 595–600 (2004).
[11]D. Shulz-Ertner, C. Karger, A. Feuerhake, A. Nikoghosyan, S. Combs, O. Jäkel, L. Edler, M. Scholz, and J. Debus, "Effectiveness of carbon ion radiotherapy in the treatment of skull-base chordomas," Int. J. Radiat. Oncol., Biol., Phys. **68**, 449–457 (2007).
[12]T. Furukawa, T. Inaniwa, S. Sato, T. Tomitani, S. Minohara, K. Noda, and T. Kanai, "Design study of a raster scanning system for moving target irradiation in carbon-ion radiotherapy," Med. Phys. **34**, 1085–1097 (2007).
[13]B. Clasie, A. Wroe, H. Kooy, N. Depauw, J. Flanz, H. Paganetti, and A.

Rosenfeld, "Assessment of out-of-field absorbed dose and equivalent dose in proton fields," Med. Phys. **37**, 311–321 (2010).
[14]International Commission on Radiological Protection, The 2007 Recommendations of the International Commission on Radiological Protection: ICRP Publication 103, Ann. ICRP **37**(2–4), 1–332 (2007).
[15]U. Schneider, A. Lomax, and B. Timmermann, "Second cancers in children treated with modern radiotherapy techniques," Radiother. Oncol. **89**, 135–140 (2008).
[16]J. Fontenot, A. Lee, and W. Neuhauser, "Risk of secondary malignant neoplasms from proton therapy and intensity-modulated x-ray therapy for early-stage prostate cancer," Int. J. Radiat. Oncol., Biol., Phys. **74**(2), 616–622 (2009).
[17]P. Taddei, D. Mirkovic, J. Fontenot, A. Giebeler, Y. Zheng, D. Kornguth, R. Mohan, and W. Newhauser, "Stray radiation dose and second cancer risk for a pediatric patient receiving craniospinal irradiation with proton beams," Phys. Med. Biol. **54**, 2259–2275 (2009).
[18]G. Mesoloras, G. A. Sandison, R. D. Stewart, J. B. Farr, and W. C. Hsi, "Neutron scattered dose equivalent to a fetus from proton radiotherapy of the mother," Med. Phys. **33**, 2479–2490 (2006).
[19]H. Jiang, B. Wang, X. G. Xu, H. D. Suit, and H. Paganetti, "Simulation of organ-specific patient effective dose due to secondary neutrons in proton radiation treatment," Phys. Med. Biol. **50**, 4337–4353 (2005).
[20]A. Wroe, B. Clasie, H. Kooy, J. Flanz, R. Schulte, and A. Rosenfeld, "Out-of-field dose equivalents delivered by passively scattered therapeutic proton beams for clinically relevant field configurations," Int. J. Radiat. Oncol., Biol., Phys. **73**, 306–313 (2009).
[21]A. Wroe, A. Rosenfeld, and R. Schulte, "Out-of-field dose equivalents delivered by proton therapy of prostate cancer," Med. Phys. **34**, 3449–3456 (2007).
[22]International Commission on Radiation Units and Measurement, "Microdosimetry," ICRU Report No. 36, 1983.
[23]H. H. Rossi and M. Zaider, *Microdosimetry and its Applications* (Springer-Verlag, Berlin, 1996).
[24]A. J. Waker, "Principles of experimental microdosimetry," Radiat. Prot. Dosim. **61**, 297–300 (1995).
[25]M. Takada, M. Baba, H. Yamaguchi, and K. Fujitaka, "Differential absorbed dose distributions in lineal energy for neutrons and gamma rays at the mono-energetic neutron calibration facility," Radiat. Prot. Dosim. **114**, 481–490 (2005).
[26]Y. Kase, T. Kanai, N. Matsufuji, Y. Furusawa, T. Elsässer, and M. Scholz, "Biophysical calculation of cell survival probabilities using amorphous track structure models for heavy-ion," Phys. Med. Biol. **53**, 37–59 (2008).
[27]H. Nose, Y. Kase, N. Matsufuji, and T. Kanai, "Field size effect of radiation quality in carbon therapy using passive method irradiation," Med. Phys. **36**, 870–875 (2009).
[28]J. F. Dicello, H. I. Amols, M. Zaider, and G. Tripard, "A comparison of microdosimetric measurements with spherical proportional counter and solid-state detectors," Radiat. Res. **82**, 441–453 (1980).
[29]M. Zaider, J. F. Dicello, D. J. Brenner, M. Takai, and M. R. Raju, "Microdosimetry of range-modulated beams of heavy ions," Radiat. Res. **87**, 511–520 (1981).
[30]International Commission on Radiation Unit and Measurements, "The quality factor in radiation protection," ICRU Report No. 40, 1986.
[31]International Commission on Radiation Unit and Measurements, "Quantities and units in radiation protection dosimetry," ICRU Report No. 51, 1993.
[32]International Commission on Radiation Unit and Measurements, "Fundamental quantities and units for ionizing radiation," ICRU Report No. 60, 1998.
[33]International Commission on Radiological Protection, The 1990 Recommendations of the International Commission on Radiological Protection: ICRP Publication 60, Ann. ICRP **21**(1–3), 1–201 (1990).
[34]K. H. Folkerts, H. G. Menzel, H. Schuhmacher, and E. Arend, "TEPC radiation protection dosimetry in the environment of accelerators and at nuclear facilities," Radiat. Prot. Dosim. **23**, 261–264 (1988).
[35]Y. Zheng, W. Newhauser, J. Fontenot, P. Taddei, and R. Mohan, "Monte Carlo study of neutron dose equivalent during passive scattering proton therapy," Phys. Med. Biol. **52**, 4481–4496 (2007).
[36]M. F. Moyers, E. R. Benton, A. Ghebremedhin, and G. Coutrakon, "Leakage and scatter radiation from a double scattering based proton beamline," Med. Phys. **35**, 128–144 (2008).
[37]J. C. Polf and W. D. Newhauser, "Calculations of neutron dose equivalent exposures form range-modulated proton therapy beams," Phys. Med. Biol. **50**, 3859–3873 (2005).
[38]H. Tomura, T. Kanai, A. Higashi, Y. Futami, N. Matsufuji, M. Endo, F. Soga, and K. Kawachi, "Analysis of the penumbra for uniform irradiation fields delivered by a wobbler method," Jpn. J. Appl. Phys., Part 1 **18**, 42–56 (1998).
[39]S. Yonai, N. Kanematsu, M. Komori, T. Kanai, Y. Takei, O. Takahashi, Y. Isobe, M. Tashiro, H. Koikegami, and H. Tomita, "Evaluation of beam wobbling methods for heavy-ion radiotherapy," Med. Phys. **35**, 927–938 (2008).
[40]A. M. Koehler, R. J. Schneider, and J. M. Sisterson, "Flattening of proton dose distributions for large-field radiotherapy," Med. Phys. **4**, 297–301 (1977).
[41]S. F. Kry, M. Salehpour, D. S. Followill, M. Stovall, D. A. Kuban, R. A. White, and I. I. Rosen, "The calculated risk of fatal secondary malignancies from intensity-modulated radiation therapy," Int. J. Radiat. Oncol., Biol., Phys. **62**(4), 1195–1203 (2005).
[42]S. F. Kry, M. Salehpour, D. S. Followill, M. Stovall, D. A. Kuban, R. A. White, and I. I. Rosen, "Out-of-field photon and neutron dose equivalents from step-and-shoot intensity-modulated radiation therapy," Int. J. Radiat. Oncol., Biol., Phys. **62**(4), 1204–1216 (2005).
[43]S. F. Kry, D. Followell, R. A. White, M. Stovall, D. A. Kuban, and M. Salehpour, "Uncertainty of calculated risk estimates for secondary malignancies after radiotherapy," Int. J. Radiat. Oncol., Biol., Phys. **68**(4), 1265–1271 (2007).
[44]Y. Nakane and Y. Sakamoto, "Measurement of absorbed dose distributions in a plastic phantom irradiated by 40- and 65-MeV quasi-monoenergetic neutrons," Nucl. Instrum. Methods Phys. Res. A **A459**, 552–564 (2001).
[45]M. Endo, H. Koyama-Ito, S. Minohara, N. Miyahara, H. Tomura, T. Kanai, K. Wawachi, H. Tsujii, and K. Morita, "HIPLAN—A heavy ion treatment planning system at HIMAC," J. Jpn. Soc. Ther. Radiol. Oncol. **8**, 231–238 (1996).
[46]R. H. Olsher, H. H. Hsu, A. Beverding, J. H. Kleck, W. H. Casson, D. G. Vasilik, and R. T. Devine, "WENDI: An improved neutron rem meter," Health Phys. **79**, 170–181 (2000).

IOP PUBLISHING PHYSICS IN MEDICINE AND BIOLOGY

Phys. Med. Biol. 55 (2010) 3545–3556 doi:10.1088/0031-9155/55/12/018

Improved dose-calculation accuracy in proton treatment planning using a simplified Monte Carlo method verified with three-dimensional measurements in an anthropomorphic phantom

Kenji Hotta[1], Ryosuke Kohno[2], Yoshihisa Takada[1], Yousuke Hara[1], Ryohei Tansho[1], Takeshi Himukai[3], Satoru Kameoka[2], Taeko Matsuura[2], Teiji Nishio[2] and Takashi Ogino[2]

[1] Institute of Applied Physics, University of Tsukuba, 1-1-1 Tennoudai, Tsukuba, Ibaraki 305-8573, Japan
[2] National Cancer Center Hospital East, 6-5-1, Kashiwanoha, Kashiwa, Chiba 277-8577, Japan
[3] National Institute of Radiological Sciences, 4-9-1, Anagawa, Inage, Chiba, 263-8555, Japan

E-mail: y-takada@bk.tsukuba.ac.jp

Received 3 February 2010, in final form 7 April 2010
Published 28 May 2010
Online at stacks.iop.org/PMB/55/3545

Abstract

Treatment planning for proton tumor therapy requires a fast and accurate dose-calculation method. We have implemented a simplified Monte Carlo (SMC) method in the treatment planning system of the National Cancer Center Hospital East for the double-scattering beam delivery scheme. The SMC method takes into account the scattering effect in materials more accurately than the pencil beam algorithm by tracking individual proton paths. We confirmed that the SMC method reproduced measured dose distributions in a heterogeneous slab phantom better than the pencil beam method. When applied to a complex anthropomorphic phantom, the SMC method reproduced the measured dose distribution well, satisfying an accuracy tolerance of 3 mm and 3% in the gamma index analysis. The SMC method required approximately 30 min to complete the calculation over a target volume of 500 cc, much less than the time required for the full Monte Carlo calculation. The SMC method is a candidate for a practical calculation technique with sufficient accuracy for clinical application.

(Some figures in this article are in colour only in the electronic version)

1. Introduction

In proton tumor therapy, tumor control while sparing adjacent organs requires a good treatment plan to maximize dose delivery to the target volume. The optimum plan is formulated by

evaluating the calculation results for a variety of beam configurations. The dose-calculation method must be fast and accurate.

Many facilities currently use pencil beam algorithms (PBAs) (Petti 1992, Hong 1996, Szymanowski 2001) for treatment planning. The required calculation time is relatively short and the accuracy of these algorithms is reasonable when the tumor is surrounded by structures of intermediate complexity. PBAs express the dose distribution formed by a mono-energetic proton pencil beam as a product of the depth-dose distribution in water obtained from measurements or Monte Carlo calculations and an off-axis radial function defined as a two-dimensional Gaussian function with an rms value determined by scattering in the materials along its central axis. The dose distributions of multiple pencil beams at various incident positions and energies are summed to obtain the dose distribution in the patient. Kohno *et al* developed a Range-Modulated-Pencil-Beam Algorithm (RMPBA) to shorten the calculation time while maintaining accuracy by using a measured depth-dose distribution for the combined beam rather than summing the contribution of protons at each specific energy (Kohno 2001).

Though PBAs perform well for homogeneous targets, the accuracy is decreased in targets with large lateral heterogeneity. Since the PBAs assume that the central axis is a straight line and determine the energy deposit and the lateral spread due to materials along the central axis, they do not include the effects of lateral density heterogeneity on the dose distribution. The PBAs also use a zero-thickness collimator approximation ignoring the edge scattering in the aperture collimator. These limitations decrease the dose-calculation accuracy of PBAs in heterogeneous media. In order to improve accuracy, Kanematsu *et al* developed a PBA variant that subdivides the pencil beam kernels into sub-pencil beams when it encounters a large heterogeneity (Kanematsu 2009).

The clinical application of full Monte Carlo calculations such as MCNPX (Waters 2002) or Geant4 (Agostinelli 2003) has been investigated (Paganetti 2008). Although they are capable of more accurately computing dose distribution, they require a long calculation time, up to 6 h per patient even using more powerful cluster machine than ours (Paganetti 2008). To reduce the calculation time, fast pseudo-Monte-Carlo algorithms were proposed (Li 2005, Yepes 2009).

Sakae *et al* (2000) developed a simplified Monte Carlo (SMC) method to obtain fast and accurate dose calculation in heterogeneous targets, and the accuracy of the method in simple targets was verified by Kohno *et al* (2002, 2003). Since the SMC method tracks individual particles, it includes lateral density heterogeneity effects on the dose distribution. A second advantage of the SMC method is easy implementation since it can use same input data for PBAs.

We implemented the SMC method in the clinical treatment planning system of the National Cancer Center Hospital East (NCCHE, Japan). We demonstrated the effectiveness of the SMC method by comparing the calculation results with measurement results in a heterogeneous slab phantom, and that in an anthropomorphic phantom simulating the complexity encountered in a clinical situation. The SMC results were also compared to RMPBA calculations. The data were analyzed using a number of methods, including a variant of the γ-index method (Low 1998) with an accuracy tolerance of 3 mm and 3%.

2. Materials and methods

2.1. Calculation model

A right-handed Cartesian system was used for dose-calculation coordinates in which the central beam axis coincided with the z-axis and the gantry rotated about the y-axis. Target data

in the original CT coordinate system were transformed into the dose-calculation coordinate system using the gantry and couch rotation angles.

The SMC method begins tracking individual protons at the entrance to the range compensator (RC). The initial beam parameters were provided by the effective-source model with the model parameters determined by measurements (Hong 1996, Symanovski 2001). The model provides the standard deviation of the initial angular distribution at any point on the entrance plane. The proton fluence distribution was based on the lateral-dose distribution measured without the RC and aperture collimator. In the system arrangement at the NCCHE, the RC is placed upstream of a patient-aperture collimator. For calculation of range loss and scattering of individual protons in material, polyethylene RC and 60 mm thick brass aperture collimator were divided into segments with a thickness of 1 mm along the z-axis. Patient volume was divided into cubic voxels with twice the edge length of the CT pixels. Each particle was characterized in terms of position, the direction expressed by the two projection angles, and the residual range in water. The trajectory of each particle was tracked by assuming multiple Coulomb scattering with scattered projection angles expressed as a normal random number with a standard deviation calculated using the Highland formula (Highland 1975, 1979). The energy loss of a proton in a segment of material was calculated using the water equivalent model (Chen 1979). We assumed that the relative dose deposit in a patient voxel could be obtained from the measured depth-dose distribution in water. One reason for the shorter calculation time of the SMC method compared with full Monte Carlo methods is the simplification in which the dose deposit in materials is calculated using the measured depth-dose distribution for a mono-energetic proton beam in water, and ignoring absorption and lateral scattering due to nuclear reaction. Note that use of the measured depth-dose curve in water implicitly includes some averaged effects from nuclear interactions.

The calculation method was compared to the RMPBA with the measured effective source model.

2.2. *Experiment*

We verified the calculation accuracy of the SMC method by comparing the calculation results with the measured dose distributions in the heterogeneous phantoms described in sections 2.2.1 and 2.2.2. The proton beam was extracted from the 235 MeV cyclotron at the NCCHE. For some experiments the energy was reduced using the energy-selection-system (ESS), and the beam was transferred to a passive beam spreading system using the double-scattering method (Nishio 1999, Tachikawa 1999).

A PTW 2D Array seven29^{TM} was used for dose detection. This is a two-dimensional detector matrix containing 729 ionization chambers in a 10 mm pitch 27 $\times$ 27 array developed by ®PTW Freiburg GmbH. Spezi reported the successful application of this detector to radiation therapy and verified the performance (Spezi 2005). The sensitive volume of a unit chamber is 5 mm $\times$ 5 mm $\times$ 5 mm. The ionization chambers of the array are open to the air. The offset thickness from the entrance surface to the center of the sensitive volume is 8 mm in WEL.

To compare the calculation results and measurements under the same conditions, we corrected the calculation of depths by the offset thickness when calculating the dose distributions. We also convolved the calculation results with the detector cell size of 5 mm $\times$ 5 mm.

2.2.1. Slab phantom. The heterogeneous slab phantom depicted in figure 1 was used for evaluation of the SMC method. We investigated lateral density heterogeneity effects on dose

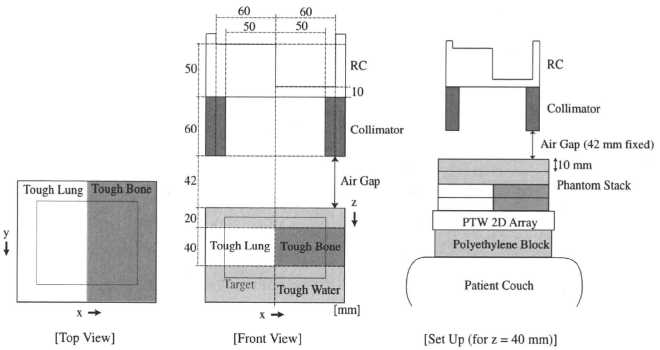

Figure 1. Experimental arrangement of heterogeneous slab phantom, RC and aperture collimator. The red line indicates the target region.

distribution using a 150 MeV proton beam passing through a ridge filter with a spread-out Bragg peak (SOBP) width of 80 mm. The phantom was constructed by combining 10 mm thick component slabs made from Tough Water (TW), Tough Lung (TL), and Tough Bone (TB) (®Kyoto Kagaku Co., Ltd). The water-equivalent–thickness ratios (Takada 2008) of TW, TL and TB are 1.01, 0.34 and 1.40, respectively. We designed the RC and the aperture collimator for the cube-shaped target with a volume of 800 cc (indicated by the red line in figure 1).

Lateral dose distributions were measured at depths of $z = 0$ mm, 20 mm, 40 mm, 60 mm, 80 mm and 90 mm. A stack of the phantom slabs was mounted on the detector to measure the dose distribution in each depth as shown in figure 1. When a different phantom stack was mounted, we fixed the distance between the aperture collimator and the phantom entrance surface by adjusting the vertical position of the patient couch. Since the chamber pitch was 10 mm, we shifted the detector by 5 mm in the x and y directions to obtain measurements with a lateral sampling pitch of 5 mm. Each measurement was repeated three times at each depth and averaged to obtain the lateral-dose distribution.

The simulation required approximately 40 min with a target voxel size of 1 mm per side using 1.14×10^8 generated protons on four cores (two dual-core 2.4 GHz AMD Opteron CPUs, four jobs running in parallel). All the dose data sets were normalized at a point ($x =$ 30 mm, $y = 60$ mm) in a flat dose region for comparison of measurements and calculations. The estimated mean statistical error of the calculated dose in the target region was 1% rms, and that of the convolved calculated dose was 0.2% rms. Reduction of the error in the convolved calculated dose came from the larger voxel size.

2.2.2. RANDO phantom. We used the head portion from a RANDO® phantom produced by the Phantom Laboratory® to simulate the complex arrangement of materials experienced in clinical applications. The RANDO phantom mimics the density distribution in the human head using resins with various compositions. Figure 2 contains the median sagittal and median horizontal CT images and the PTV. The phantom is composed of horizontal layers of 25 mm thick. We measured the dose distributions in the layers with the z-index numbered from 1

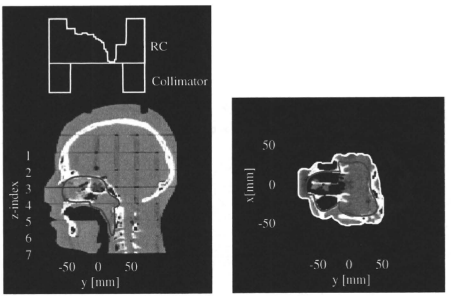

Figure 2. Median sagittal and median horizontal CT images of the head portion from the RANDO phantom. The iso-center (red cross), PTV (red line) and RC and collimator shape (white line) are also depicted.

to 7 as shown in the figure. To simulate clinical situations, we followed the actual patient treatment procedure: obtaining a CT, delineating the PTV, determining the beam direction, manufacturing the corresponding RC and aperture collimator, aligning the reference surface markers on the phantom with laser cross-hairs and irradiating the phantom on the patient couch. We designed a treatment plan assuming a head and neck cancer with a volume of approximately 500 cc. The smearing distance of the RC (Kooy 2008) was taken at 4.5 mm. Since the measurement plane was limited to the horizontal plane due to the layered structure of the phantom, the irradiation direction was also limited to downward from the top of the head. Although the results have no clinical significance due to the unrealistic selection of the irradiation direction, it simulates the dose distribution in the complex heterogeneous region typically found in the head and neck cases.

We used a 235 MeV proton beam with a SOBP width of 80 mm. We mounted a stack of phantom layers on the detector to measure the dose distribution in each measurement plane. The distance between the aperture collimator and the phantom entrance surface was fixed by adjusting the couch height, again. The reported results are the average of three measurements. To estimate the effect of set-up errors on the dose distribution, we repeated the set-up and measurement procedure three times on the $z = 4$ layer where a complicated lateral-dose distribution was expected.

The simulation required approximately 30 min when the target voxel size was 1.17 mm on a side and the number of generated particles was 4.68×10^7 on four cores (two dual-core 2.4 GHz AMD Opteron CPUs, four jobs running in parallel). All the dose data sets were normalized with reference to the dose at the iso-center for comparison. The estimated mean statistical error of the calculated dose in the target region was 1.2% rms, and that of the convolved calculated dose was 0.25% rms.

3. Results

3.1. Slab phantom

Figure 2 compares the iso-dose distributions obtained from (a) measurements, (b) the SMC calculation and (c) the RMPBA calculation. In the figure, we note that the high-dose region

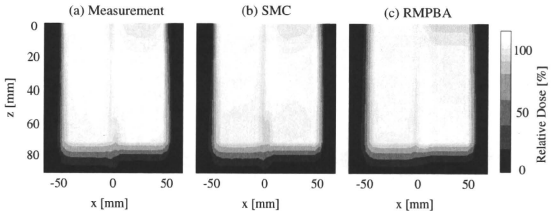

Figure 3. Iso-dose distributions in the heterogeneous slab phantom from (a) measurements, (b) the SMC and (c) the RMPBA. The measurements were obtained at $z = 0$ mm, 20 mm, 40 mm, 60 mm, 80 mm and 90 mm.

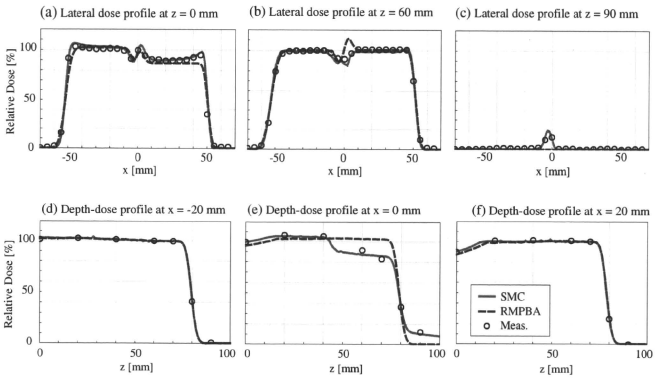

Figure 4. Dose profiles in the heterogeneous slab phantom: solid lines indicate the SMC prediction, dashed lines indicate the RMPBA prediction, and open circles represent measurements. Figures (a)–(c) are lateral-dose profiles at $z = 0$ mm, 60 mm and 90 mm. Figures (d)–(f) are depth-dose profiles at $y = -20$ mm, 0 mm and 20 mm. Since the estimated measurement error from three measurements in each set-up is less than 1.0%p-p of the normalization dose, error bars are not displayed (smaller than circles).

around $x = 0$ mm extends to a region deeper than 50 mm only in the RMPBA. Such differences of dose distribution are shown more clearly in lateral- and depth-dose profiles of figure 4. The SMC method reproduced the measurement results better than the RMPBA in three regions. The first is the peripheral high-dose region around $x = \pm 50$ mm in figure 4(a) that is influenced by the scattered and energy-degraded protons interacting with the edge of the aperture collimator. The SMC method accurately reproduced the measured dose distribution, while the RMPBA does not take into account edge-scattered proton paths and cannot reproduce the dose distribution well in this region. The second region is a dose reduction at depths between $z = 40$ mm and $z = 70$ mm in the vicinity of $x = 0$ mm (figures 4(b) and (e)). This area is influenced by protons passing through both the thicker section of the RC and the

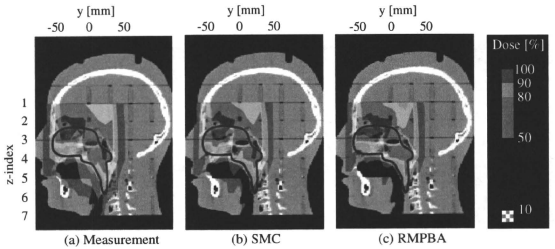

Figure 5. Median sagittal iso-dose distributions in the anthropomorphic phantom from (a) measurements, (b) the SMC and (c) the RMPBA.

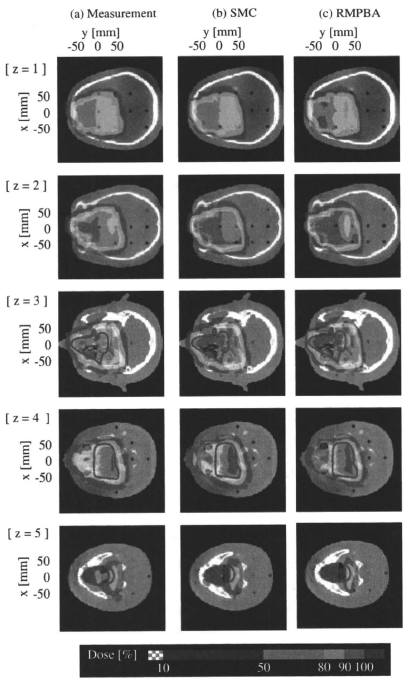

Figure 6. Horizontal iso-dose distributions in the anthropomorphic phantom. The red lines show the target region.

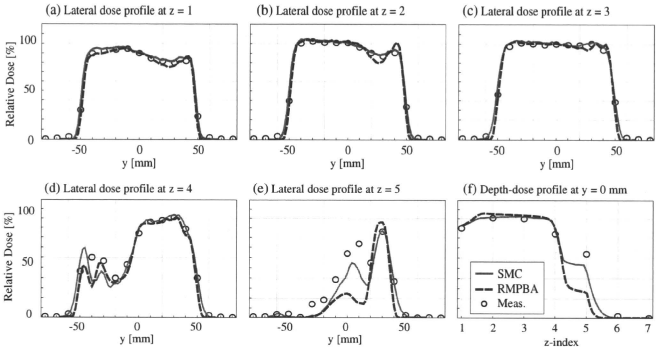

Figure 7. Lateral- and depth-dose profiles in the anthropomorphic phantom. The solid lines depict calculation results using the SMC, the dashed lines depict calculation results from the RMPBA, and the hollow circles represent measurements. Figures (a)–(e) are lateral-dose profiles on the $z = 1$, 2, 3, 4 and 5 levels, and figure (f) is a depth-dose profile at $y = 0$ mm. Since the estimated measurement error from three measurements in each set-up is less than 1.3%p-p of the normalization dose, error bars are not displayed (smaller than circles).

higher-density region in the phantom. The third region is a low-dose region near $x = 0$ mm at a depth of $z = 90$ mm (figures 4(c) and (e)) formed by protons passing through both the thinner section of the RC and the lower-density region in the phantom. Note that this region is located deeper than the target distal boundary. The RMPBA could not reproduce the dose in this region due to the disregard of irregular proton paths mentioned above while the SMC could.

Both the SMC and the RMPBA perfectly reproduced the depth-dose distribution in the region lacking lateral heterogeneity (figures 4(d) and (f)). The difference in calculation accuracy between the SMC and the RMPBA in figure 4(e) was caused by the difference in operation between the two algorithms; the SMC method tracks almost all proton paths while some paths in the RMPBA are missing.

3.2. RANDO phantom

Figures 5 and 6 describe the iso-dose distributions in the median sagittal plane and horizontal planes obtained using (a) measurements, (b) the SMC calculation and (c) the RMPBA calculation. We ignored the $z = 6$ and $z = 7$ planes because almost no protons reached these levels. The number of measurement points irradiated with more than 10% of the normalization dose was 80, 82, 88, 88 and 41 for $z = 1$ through 5. Apparent discrepancy between the target distal boundary and the dose distal boundary can be attributed to difference between the displayed depth and the measured depth by the detector with a cover thickness of 8 mm WEL. Since our interest is focused on difference between measurements and calculations, this is not a major issue here. In the figures, you will note that both the SMC and the RMPBA reproduced the overall measured distribution in some accuracy. Yet there are some local differences shown in dose profiles of figure 7: (a)–(e) are lateral profiles at $z = 1$–5, and (f) is a distal profile at

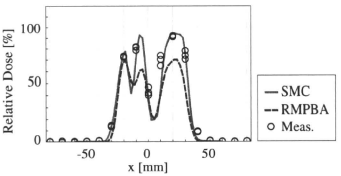

Figure 8. Effect of alignment error on dose distribution in the anthropomorphic phantom along the x-axis at $y = -20$ mm on the $z = 4$ layer. The dose errors caused by set-up misalignment are large at $x = 10$ mm and $x = 30$ mm where the dose gradient is large. Since the estimated measurement error from times measurements in each set-up is less than 0.7%p-p of the normalization dose, error bars are not displayed (smaller than circles).

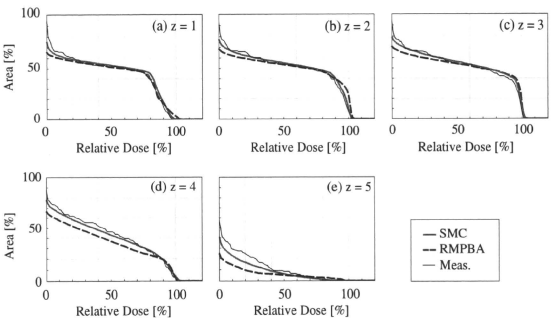

Figure 9. Comparison of dose-surface histograms in each plane from measurements, SMC calculation and PBA calculation. The black solid lines depict the measurement data, the red solid lines depict the SMC results and the blue dashed lines depict the RMPBA results.

$y = 0$ mm. Figures 4(a)–(c) show that both calculations reproduce measurements well with minor local differences. In contrast, we note large discrepancy between measurements and calculations and difference between the SMC and the RMPBA in a part of figures 4(d)–(f). The discrepancy between measurements and calculations is caused by the range uncertainty of the phantom and the large dose gradient in the distal fall-off part of the Bragg curve. The difference between the SMC and the RMPBA notably found in figures 4(e) and (f) is caused by the fact that the RMPBA disregards dose contribution of protons passing through the irregular paths along the phantom and reaching the deep region and underestimates the dose in the deep region.

We also examined the dose error caused by misalignment of the RC, aperture collimator, phantom and detector. Figure 8 depicts three lateral-dose profiles on the $z = 4$ layer of the head phantom following three separate set-up procedures. The figure also contains the SMC and the RMPBA calculation results for the case of no set-up error. The $z = 4$ layer was selected since it includes a region with a large dose gradient in the lateral direction that is

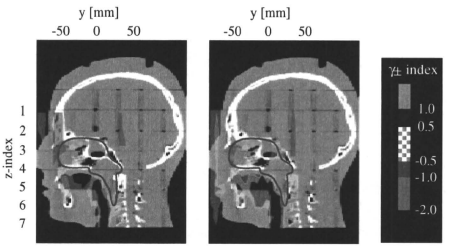

(a) SMC (b) RMPBA

Figure 10. The $\gamma_{\pm}$-index distributions in the median sagittal plane of the anthropomorphic phantom from (a) the SMC and (b) the RMPBA. The RMPBA exhibits a larger underestimated region than the SMC.

sensitive to set-up error. The measured dose error due to misalignment was a maximum of 9.2%p-p of the normalization dose. Such a large dose error can be attributed to an estimated set-up error of ± 0.5 mm and the large dose gradient. The misalignment error is consistent with error of the alignment system using laser cross-hairs.

Figure 8 compares the dose-surface histograms (DSH) obtained from measurements, the SMC calculation and the RMPBA calculation in each measurement plane. The SMC method is superior to the RMPBA, which underestimates the dose in deeper regions. The difference in calculation accuracy between the two algorithms arises from consideration or disregard of irregular proton paths in heterogeneous media. The dose underestimation observed in the $z = 5$ layer even by SMC is caused by uncertainty in the CT-value-to-range conversion and by the large low-density region representing the oral cavity present in this layer. Since most protons in this region have a small residual range, the dose in this region is very sensitive to small uncertainties in the proton range.

4. Discussion

We evaluated the calculation accuracy using the γ-index method (Low 1998). This method simultaneously evaluates the dose difference and the distance to agreement quantitatively. We newly defined a signed-gamma-index ($\gamma_{\pm}$-index) at each measurement position to differentiate between overestimation and underestimation of the dose:

$$\gamma_{\pm}(\boldsymbol{r}_m) = \frac{D_c(\boldsymbol{r}_m) - D_m(\boldsymbol{r}_m)}{|D_c(\boldsymbol{r}_m) - D_m(\boldsymbol{r}_m)|} \times \min_{\boldsymbol{r}_c} \left[\sqrt{\frac{(D_c(\boldsymbol{r}_c) - D_m(\boldsymbol{r}_m))^2}{D^2_{\text{tolerance}}} + \frac{(\boldsymbol{r}_c - \boldsymbol{r}_m)^2}{r^2_{\text{tolerance}}}} \right], \tag{1}$$

where D_m and D_c represent the measured and calculated doses, r_c and r_m are the calculated and measured positions, and the parameters $D_{\text{tolerance}}$ and $r_{\text{tolerance}}$ are the tolerance error values of the dose and the distance. The acceptable error in proton therapy dose calculation for heterogeneous targets is not clearly defined at present. We followed the recommendations of Low (1998) for photon therapy, and used 3% for $D_{\text{tolerance}}$ and 3 mm for $r_{\text{tolerance}}$ in this paper. We also defined the pass rate as the fraction of calculation points satisfying the condition of $-1 < \gamma_{\pm} < 1$.

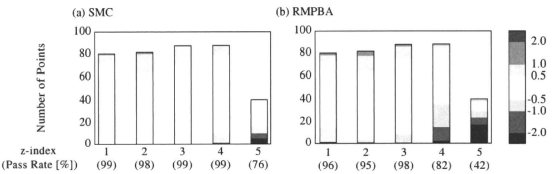

Figure 11. $\gamma_{\pm}$-index histogram for (a) the SMC and (b) the RMPBA. The $\gamma_{\pm}$-index in the stacked bar chart is shown in decreasing order from top to bottom. The number of points contained in a range of signed gamma index is indicated by the height of each bar. The pass rate is printed under the z-index.

Figure 10 illustrates the $\gamma_{\pm}$-index distributions on the median sagittal plane for (a) the SMC and (b) the RMPBA. Figure 5 contains stacked bar charts representing the $\gamma_{\pm}$-index for (a) the SMC and (b) the RMPBA. We expressed the $\gamma_{\pm}$-index scale using various intensities of red to highlight positive regions and blue for negative regions. The color intensity is proportional to the absolute value of the $\gamma_{\pm}$-index. The pass rates in individual horizontal planes are also indicated under the z-index of the measurement planes. While calculation results obtained using the SMC method agreed well with the measurement results for layers $z = 1$–4, the pass rates for the RMPBA method fell below 90% in the $z = 4$ and 5 layers due to underestimation of the dose. Therefore, the SMC method is superior in the calculation accuracy to the RMPBA. Since the SMC method can accurately reproduce the measured dose distribution in complex media within a reasonable calculation time, it is capable of improving the accuracy of dose calculations in clinical situations.

5. Conclusion

We implemented the SMC method in the treatment planning system of the NCCHE in order to improve dose-calculation accuracy in heterogeneous targets. The SMC method is easy to implement because it can use the same input data for PBAs. We verified the effectiveness of the SMC method by comparing the calculation results to the dose distributions measured at different depths in a heterogeneous slab phantom using a two-dimensional detector. We also measured the dose distributions at seven horizontal planes in an anthropomorphic phantom. For both these cases, we found that the SMC method reproduced the measured dose distributions better than the RMPBA. In the slab phantom, we found that the RMPBA overestimated the dose in shallow regions and underestimated the dose in deep regions due to disregard of some proton paths in the heterogeneous region. The same tendency was also found for the RMPBA dose calculations for the anthropomorphic phantom. Since PBAs fundamentally have a risk of disregarding some proton paths, they may underestimate the dose in deep region for the case with large heterogeneity around the target.

We evaluated the treatment plan using the $\gamma_{\pm}$-index analysis and found that the SMC method reproduced the measured dose distributions well within the accuracy tolerance of 3 mm and 3% in almost all regions. In addition, the calculation time required for the SMC method was about 30 min for a typical clinical case (target volume of 500 cc). The SMC method provides the higher calculation accuracy than RMPBA within a reasonable time, even for such a complex case. Since verification of the effectiveness of the SMC method is required

for many clinical cases, we have begun a retrospective comparison between the SMC and PBA methods using previous proton therapy cases.

Acknowledgments

We appreciate SHI Accelerator Service Ltd, for their support with the experiments.

References

Agostinelli S *et al* 2003 GEANT4: a simulation toolkit *Nucl. Instrum. Methods. Phys. Res.* A **506** 250–303

Chen G T, Singh R P, Castro J R, Lyman J T and Quivey J M 1979 Treatment planning for heavy ion radiotherapy *Int. J. Radiat. Oncol. Biol. Phys.* **5** 1809–19

Highland V L 1975 Some practical remarks on multiple scattering *Nucl. Instrum. Methods* **129** 497–9

Highland V L 1979 Some practical remarks on multiple scattering *Nucl. Instrum. Methods* **161** 171

Hong L *et al* 1996 A pencil beam algorithm for proton dose calculations *Phys. Med. Biol.* **41** 1305–30

Kanematsu N, Komori M, Yonai S and Ishizaki A 2009 Dynamic splitting of Gaussian pencil beams in heterogeneity-correction algorithms for radiotherapy with heavy charged particles *Phys. Med. Biol.* **54** 2015–27

Kohno R *et al* 2001 Range-modulated pencil beam algorithm for proton dose calculations *Jpn. J. Appl. Phys.* **40** 5187–93

Kohno R *et al* 2002 Simplified Monte Carlo dose calculation for therapeutic proton beams *Jpn. J. Appl. Phys.* **41** L294–7

Kohno R *et al* 2003 Experimental evaluation of validity of simplified Monte Carlo method in proton dose calculations *Phys. Med. Biol.* **48** 1277–88

Kooy H M, Trofimov A, Engelsman M and Smith A R 2008 Treatment planning *Proton and Charged Particle Radiotherapy* ed T F Delaney and H M Kooy (Philadelphia, PA: Lippincott Williams & Wilkins) chapter 8, pp 70–107

Li J S, Shahine B, Fourkal E and Ma C M 2005 A particle track-repeating algorithm for proton beam dose calculation *Phys. Med. Biol.* **50** 1001–10

Low D A, Harms W B, Mutic S and Purdy J A 1998 A technique for the quantitative evaluation of dose distributions *Med. Phys.* **25** 656–61

Nishio T *et al* 2006 Development of a simple control system for uniform proton dose distribution in a dual-ring double scattering method *Phys. Med. Biol.* **51** 1249–60

Paganetti H *et al* 2008 Clinical implementation of full Monte Carlo dose calculation in proton beam therapy *Phys. Med. Biol.* **53** 4825–53

Petti P L 1992 Differential-pencil beam dose calculations for charged particles *Med. Phys.* **19** 137–49

Schaffner B, Pedroni E and Lomax A 1999 Dose calculation models for proton treatment planning using a dynamic beam delivery system: an attempt to include density heterogeneity effects in the analytical dose calculation *Phys. Med. Biol.* **44** 27–41

Sakae T *et al* 2000 Multi-layer energy filter for realizing conformal irradiation in charged particle therapy *Med. Phys.* **27** 368–373

Spezi E, Angelini A L, Romani F and Ferri A 2005 Characterization of a 2D ion chamber array for the verification of radiotherapy treatments *Phys. Med. Biol.* **50** 3361–73

Szymanowski H *et al* 2001 Experimental determination and verification of the parameters used in a proton pencil beam algorithm *Med. Phys.* **28** 975–87

Tachikawa T *et al* 1999 Proton beam therapy facilities of the National Cancer Center East Hospital *Radiat. Indust.* **84** 48–53

Takada Y *et al* 2008 The basic study of a bi-material range compensator for improving dose uniformity for proton therapy *Phys. Med. Biol.* **53** 5555–69

Waters L 2002 MCNPX user's manual version 2.4.0 *Los Alamos National Laboratory Report* LA-CP-02-408

Yepes P, Randeniya S, Taddei P and Newhauser W 2009 Monte Carlo fast dose calculator for proton radiotherapy: application to a voxelized geometry representing a patient with prostate cancer *Phys. Med. Biol.* **54** N21–8

Int. J. Radiation Oncology Biol. Phys., Vol. 76, No. 1, pp. 277–286, 2010

0360-3016/10/$–see front matter

ELSEVIER

doi:10.1016/j.ijrobp.2009.05.065

PHYSICS CONTRIBUTION

THE DEVELOPMENT AND CLINICAL USE OF A BEAM ON-LINE PET SYSTEM MOUNTED ON A ROTATING GANTRY PORT IN PROTON THERAPY

TEIJI NISHIO, PH.D.,*† AYA MIYATAKE, M.SC.,‡ TAKASHI OGINO, M.D.,* KEIICHI NAKAGAWA, M.D.,† NAGAHIRO SAIJO, M.D.,§ AND HIROYASU ESUMI, M.D.||

From the * Particle Therapy Division, Research Center for Innovative Oncology, National Cancer Center, Kashiwa; † Department of Radiology, Graduate School of Medicine, University of Tokyo; ‡ Department of Nuclear Engineering and Management, Graduate School of Engineering, University of Tokyo; § Deputy Director, National Cancer Center, Kashiwa; and || Director, National Cancer Center, Kashiwa

Purpose: To verify the usefulness of our developed beam ON-LINE positron emission tomography (PET) system mounted on a rotating gantry port (BOLPs-RGp) for dose–volume delivery-guided proton therapy (DGPT).
Methods and Materials: In the proton treatment room at our facility, a BOLPs-RGp was constructed so that a planar PET apparatus could be mounted with its field of view covering the iso-center of the beam irradiation system. Activity measurements were performed in 48 patients with tumors of the head and neck, liver, lungs, prostate, and brain. The position and intensity of the activity were measured using the BOLPs-RGp during the 200 s immediately after the proton irradiation.
Results: The daily measured activity images acquired by the BOLPs-RGp showed the proton irradiation volume in each patient. Changes in the proton-irradiated volume were indicated by differences between a reference activity image (taken at the first treatment) and the daily activity-images. In the case of head-and-neck treatment, the activity distribution changed in the areas where partial tumor reduction was observed. In the case of liver treatment, it was observed that the washout effect in necrotic tumor cells was slower than in non-necrotic tumor cells.
Conclusions: The BOLPs-RGp was developed for the DGPT. The accuracy of proton treatment was evaluated by measuring changes of daily measured activity. Information about the positron-emitting nuclei generated during proton irradiation can be used as a basis for ensuring the high accuracy of irradiation in proton treatment. © **2010 Elsevier Inc.**

Dose–volume delivery guided proton therapy (DGPT), Beam ON-LINE PET system on rotating gantry port (BOLPs-RGp), Target nuclear fragment reaction.

INTRODUCTION

Proton therapy is a form of radiotherapy that enables the concentration of a dose onto a tumor by the use of a scanned or modulated Bragg peak. Therefore, it is very important to evaluate the proton-irradiated volume accurately.

Recently, to ensure the high accuracy of proton therapy, imaging studies of positron-emitting nuclei that are generated by target nuclear fragment reactions involving incident protons and nuclei from a patient's body have been performed (1–14). The annihilation gamma rays from the positron-emitting nuclei were measured by a positron emission tomography (PET) system (specifically a beam OFF-LINE PET system using commercial PET apparatus or PET-computed tomography [CT] apparatus postirradiation or a beam ON-LINE PET system in a proton treatment room). The beam OFF-LINE PET system using the commercial PET-CT apparatus has the advantage of being able to easily acquire fusion images and the ability to reconstruct three-dimensional images. However, the time required for the movement of the patient to the PET room (10–30 min) and the resulting deterioration of the statistical accuracy of the acquired data are large disadvantages. With the beam ON-LINE PET system, capturing a large view and the acquisition of three-dimensional images are difficult because of geometrical problems caused by the beam direction and the PET apparatus (7, 15, 16).

Reprint requests to: Teiji Nishio, Ph.D., Particle Therapy Division, Research Center for Innovative Oncology, National Cancer Center, Kashiwa 6-5-1 Kashiwano-ha, Kashiwa-shi, Chiba 277-8577, Japan. Tel: (+81) 4-7133-1111; Fax: (+81) 4-7134-7048; E-mail: tnishio@east.ncc.go.jp

Conflict of interest: none.

Supported by Health and Labour Science Research Grants from the Japanese Government.

Acknowledgment—The authors would like to thank the staff members of the Proton Radiotherapy Department of the National Cancer Center, Kashiwa for their help and the members of SHI Accelerator Service, Ltd., and Accelerator Engineering, Inc., for operating of the proton apparatus. We also acknowledge T. Okamoto of Hamamatsu Photonics, K. K., T. Tachikawa of Sumitomo Heavy Industries, Ltd., and H. Oka of SGI Japan, Ltd., for their technical support.

Received Jan 6, 2009, and in revised form May 28, 2009. Accepted for publication May 29, 2009.

The ability to take daily PET images with a high statistical accuracy while the patient remains in the proton irradiation room is a large advantage. Besides, availability of a cone beam (CB) CT system or CT apparatus in the irradiation room can offer the possibility of daily and in situ monitoring of the patient's anatomy. A prototype beam ON-LINE PET system (BOLPs) was previously constructed for basic research (10), and verification of the proton-irradiated volume in a patient's body was confirmed using a PET apparatus and a PET-CT apparatus (beam OFF-LINE PET system) (13).

A BOLPs mounted on a rotating gantry port (BOLPs-RGp) was constructed in our proton treatment room. Activity measurement and PET imaging were performed in 48 patients with tumors of the head and neck, liver, lungs, prostate, and brain during proton treatment at our facility. The position and intensity of the activity were measured daily using the BOLPs-RGp immediately after proton irradiation. Using the activity measurement, we were able to confirm whether the proton beam irradiation of the tumor was reproducibly performed during the treatment period. Moreover, changes in the activity distribution were observed as the volume of the tumor changed, and these changes were related to the delivery dose, changes in the body shape and position of the patient, and the physiologic changes. The PET images from the BOLPs-RGp were sufficient to provide high-quality proton treatment.

METHODS AND MATERIALS

Design of a beam ON-LINE PET system mounted on an RGp

Via the detection of pairs of annihilation gamma rays emitted from the generated radioactive nuclei of a patient's body, the BOLPs-RGp is designed to determine the position and activity of the positron-emitting nuclei generated in patients by proton irradiation. Figure 1 is a picture of the BOLPs-RGp. The BOLPs-RGp was developed as a standardized system for use with proton therapy devices. During proton therapy, the detector heads have many degrees of freedom and the system allows remote control adaptation to each new proton beam condition and a patient's position. As a result, the measurement of the activity distribution is simple.

A planar positron imaging system (Hamamatsu Photonics K. K., Hamamatsu, Japan) (17) was newly arranged for the BOLPs-RGp. In comparison to the system used previously (10), the 24 detector units mounted on each detector head were increased to 36 detector units, and each unit was composed of 11 × 10 arrays of BGO ($Bi_4Ge_3O_{12}$) crystals with a crystal size of 2 × 2 × 20 mm^3. Furthermore, the 2,400 crystals were increased to 3,600 crystals. The gap of each unit became 3.3 mm from 11.0 mm for minimizing dead space in the detector. The field of view (FOV) became 164.8 × 167.0 mm^2 from 120.8 × 186.8 mm^2. The maximum field size is 185.0 × 185.0 mm^2 in the rotating gantry port with the BOLPs-RGp. Therefore, the FOV can almost cover each treatment site of the head and neck, liver, lungs, prostate, and brain for a proton treatment in our facility. However, in case of prostate, the depth activity distribution is not measured in the entrance of the incident proton beam. The BOLPs-RGp was mounted on and the center of its detection area was aligned with the iso-center of the rotating gantry in the treatment room of the proton therapy facility at our center. A PET image reconstructed by a back-projection method

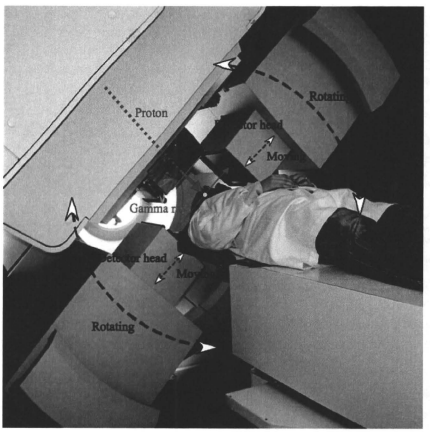

Fig. 1. Setup of the BOLPs-RGp, which is mounted on the rotating gantry port of our proton treatment room.

along the axis of the proton beam direction is always included in the FOV of the opposing detectors together with the axis of the rotating angle of the gantry system. The distance between the two opposing detector heads of the BOLPs-RGp can be adjusted from 30 to 100 cm. When the activity is not being measured, the detector head is stored inside the wall of the gantry device. The position resolution of this system is about 2 mm for the full width at half maximum in the case of use of ^{22}Na point source. The maximum data collection rate for the coincident detection of pair annihilation gamma rays is about 4,000 counts/s/cm^2 (kcps/cm^2). The accuracy of the measurements of activity distribution by this system was verified by a prototype beam ON-LINE PET system (10). The measured data are stored using in the software's list mode format. The activity image is renewed every second. The information of the on-off time points of beam irradiation is recorded in the data, and the image can be restructured according to this information. The PET data from the irradiation field of each patient are managed throughout each treatment day.

The detection efficiency of the distance between the detector heads was calibrated by using the thin-flat acrylic container filled with ^{18}F-solution. The calibration is used for a correction of the imaging uniformity and the detection sensitivity. The attenuation coefficient of 511-keV gamma rays in the patient's body was calculated by the patient's CT image data. They are used for a construction of the activity imaging. The correction of the photon scattering in the patient's body is not considered for the activity imaging. Furthermore, the photons scattered in the patient's body outside the FOV are detected by the effect of the geometry of the detector head. Therefore, the activity image is contaminated by about 10% background in this system. As the result, the position resolution of the activity distribution will become large more than 2 mm in the clinical case of a proton therapy.

Activity measurement in a patient during proton treatment

The measurement of activity was performed daily in 48 cases involving tumors of the head and neck, liver, lungs, prostate, and brain

using the BOLPs-RGp. The position and intensity of activity were measured during the 200 s immediately after proton irradiation using the trigger signal of the beam-off time. The measurement was performed using the shortest possible distance between the two opposing detector heads of the BOLPs-RGp for each patient. The average distance of the detector heads was 40 cm for the head and neck and the brain, 70 cm for the liver and the lungs, and 50 cm for the prostate. The time of 200 s after proton beam irradiation was chosen according to the intensity of activity estimated from the results of other studies (10, 13). The activity data obtained during proton irradiation were not used for PET imaging. Various types of background radiation (X-rays, gamma rays, and neutrons) occur during proton beam irradiation, and the quality of the activity image becomes markedly worse in their presence (2, 10, 15, 16). Furthermore, high radiation decreases the accuracy of the detector.

Verification of activity measurement was performed in 18, 4, 15, 10, and 1 cases involving tumors of the head and neck, the liver, the lungs, the prostate, and the brain, respectively. The typical fractional dose is 2.5 Gy equivalents (GyE = Gy × the relative biologic effectiveness: [= 1.1 = constant]) for the head and neck, 3.8 GyE for the liver, 4.0 GyE for the lungs, 2.0 GyE for the prostate, and 2.5 GyE for the brain in our facility. The irradiated field is typically planned with three fields in the head and neck and two fields in other sites. Furthermore, the typical number of irradiated field per fractional dose is one in the head and neck, liver, and prostate, and two in the lungs. The fractional dose was delivered over an irradiation time of 10–300 s. The proton beam irradiation was synchronized with the organ motion caused by respiration in the liver and the lungs.

Procedure for clinical use of activity image

A flow chart of procedure for clinical use of the BOLPs-RGp is shown in Fig. 2. In the clinical use, the main operation is to take an activity image every day and compare the activity image of the first day of treatment with each activity image during the comparatively long period of the treatment. If the difference of both the images is confirmed by reducing of the tumor size and changing of the body shape, then the new dose distribution is obtained from redose calculation of the plan on a new CT image acquisition, and the first proton treatment plan is immediately corrected to the new plan. As a result, proton treatments of high accuracy can be offered to the patient by keeping of the planned dose delivery.

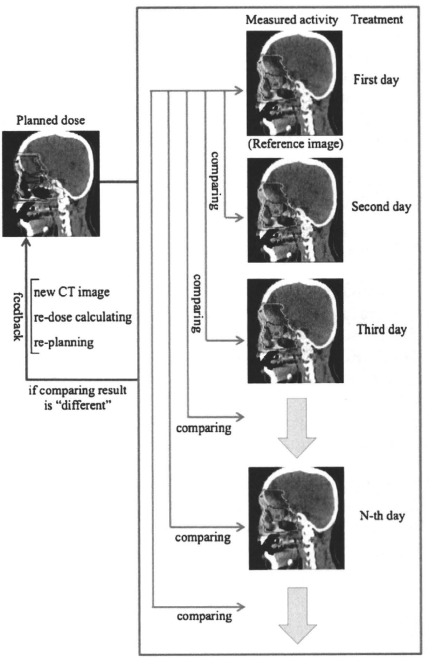

Fig. 2. Flow diagram of the procedure for the clinical use of the BOLPs-RGp.

RESULTS

Estimation of the measurement time for PET imaging

An estimation of an appropriate measurement time for PET imaging was performed using the measured activity data from tumors of the head and neck. The proton beam conditions were as follows: an energy of 120 MeV, a spread out of Bragg peak (SOBP) of 80-mm width, a gantry angle of 340°, a fractional dose of 2.5 GyE, and an irradiation time of 24 s. The distance between the detector heads was 70 cm, and the detection rate of the activity was 1.5 kcps. The left panel of Fig. 3 shows the number of detection events per volume during the detection period after proton beam irradiation. The statistical error (= standard deviation/mean value) decreased as the detection time increased. The error was 2.8% for a 200-s detection time, 3.0% for 150 s, 3.4% for 100 s, and 4.4% for 50 s. The right panel of Fig. 3 shows PET images taken using detection times of (a) 0, (b) 50, (c) 100, and (d) 200 s.

PET images of each treatment site

Typical PET images obtained by the BOLPs-RGp are shown for each case involving tumors of the head and neck, the liver, the lungs, the prostate, and the brain. Figure 4 shows the calculated dose distribution and the measured activity distribution on the first treatment day. The beam irradiation parameters were shown in Table 1. The PET images were obtained during the 200 s after proton beam irradiation. The mean detection rates of the activity generated in the proton beam irradiated volume were 1.58, 1.39, 0.53, 1.08, and 1.85 kcps, respectively. The color line and wash normalized to the iso-center show the dose distribution and activity distribution, respectively. By comparing and verifying between the calculated dose distribution and the measured activity distribution, it can be confirmed visually and roughly that the proton beam has irradiated the tumor. In cases of the liver and the lungs, the length of beam irradiation time is adjusted according to the stability of respiration on the treatment day and the patient. By the effect of organ motion, the number of

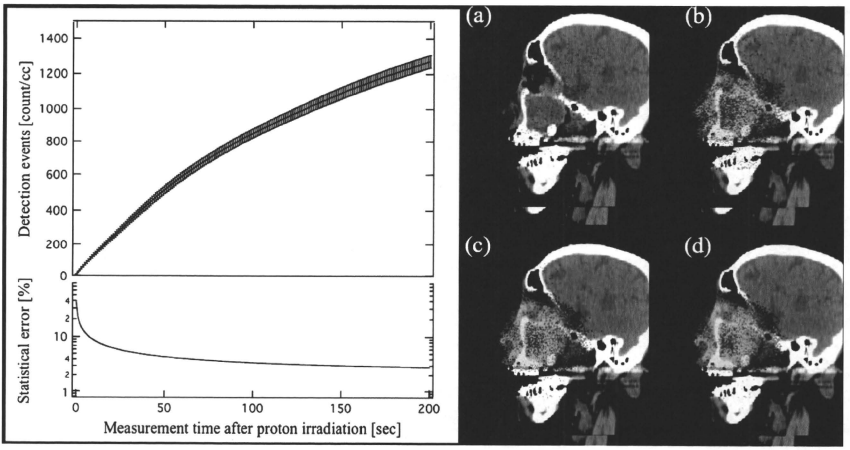

Fig. 3. The number of detection events per volume and PET images obtained during the detection period after proton beam irradiation. The PET images for detection period of (a) 0, (b) 50, (c) 100, and (d) 200 s are shown.

the detection event of the activity measured in the gating window will became about one third of the total detection events, and the statistical error will increase. Therefore, the measurement was performed with no synchronization with organ motion by respiration.

Changes in the activity distribution during the treatment period

In each treatment site, the activity distribution changed probably by reduction of the tumor size and changing of the body shape was conspicuously observed in some cases of the head and neck.

The verification was performed for a case involving tumors of the head and neck. Proton beam irradiation was performed in three fields of view: Port 1: 123 MeV, 90-mm SOBP, 350° gantry angle, 0° bed angle; Port 2: 121 MeV, 90-mm SOBP, 10° gantry angle, 20° bed angle; and Port 3: 117 MeV, 80-mm SOBP, 340° gantry angle, 350° bed angle. The irradiation dose was 2.5 GyE. Figure 5 shows a calculated proton dose distribution, an activity distribution, and a depth profile of a 2.5-GyE dose irradiation after a delivery dose of 2.5 (reference image), 10.0, 17.5, or 32.5 GyE from Port 1, a delivery dose of 5.0 (reference image), 12.5, 20.0, or 35.0 GyE, from Port 2, and a delivery dose of 7.5 (reference image), 15.0, 22.5, or 30.0 GyE from Port 3. Changes of the activity distribution were observed according to changes of the proton beam range and the dose delivered by previous irradiations resulted in a reduction of the tumor (see the arrow and the area surrounded by the dotted line in Fig. 5). The changing values of the activity range for each irradiation field (Port 1, Port 2, and Port 3) are shown in upper left of Fig. 6. The activity range was defined by the depth point of 50% distal falloff in the activity distribution normalized at the iso-center. The changing value of the activity range fully exceeded a 10-mm length. Moreover, to observe the changes in the activity distribution in the depth direction in a similar manner, the ratio of the integration of the detected numbers between 20 mm and 70 mm from the iso-center was expressed as follows:

$$R(D) = \frac{\int_{20}^{70} \left(dA(D)/dZ \right) dz}{\int_{20}^{70} \left(dA(0)/dZ \right) dz}. \quad (1)$$

Here, z is the depth, D is the delivery dose, A(D) is the depth activity distribution, and A(0) is the reference depth activity distribution. The ratio of the delivery dose is shown in the middle left of Fig. 6. The bottom left of Fig. 6 is the proton beam irradiation time per fraction dose at each irradiation. The average of the irradiation time was 30 s, and the difference of the irradiation time at random was within 3 s.

In this case, a new CT image was scanned and a retreatment planning was produced after the delivery of 35 GyE of the prescribed dose of 65 GyE. The volume of the tumor was decreased from 184 mL to 125 mL (the arrow in right of Fig. 6 shows the visible tumor reduction), and the maximum beam range was shortened by 20-mm water equivalent length. In the other 2 cases of 18 clinical cases of the head and neck, the changing activity range of more than 10 mm was observed. Similarly, the new CT image acquisition and the retreatment planning were immediately performed after the observation of the changing activity range. The reduction

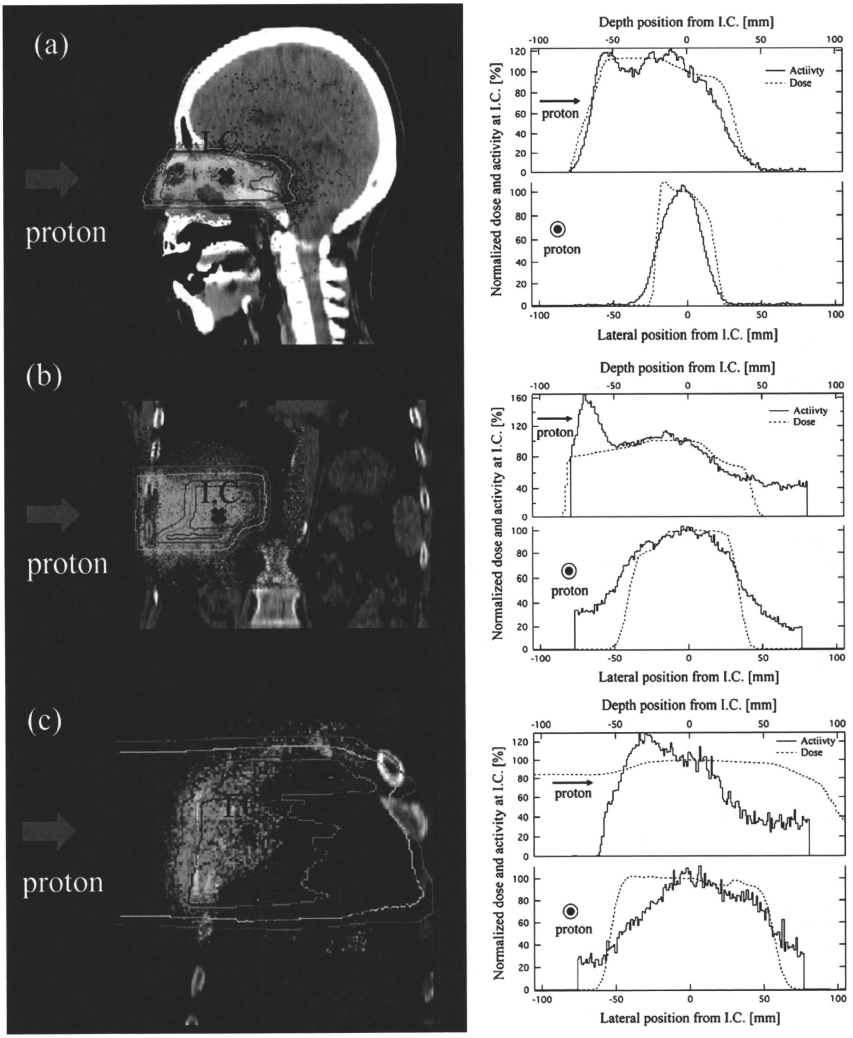

Fig. 4. The calculated dose distribution and the measured activity distribution (left figure), and corresponding lateral and depth profiles (right figure) of the irradiation fields (see Table 1) in each case involving tumors of the head and neck (a), the liver (b), the lungs (c), the prostate (d), and the brain (e), respectively. The iso-dose line of 100% is red, 80% yellowish green, 50% light blue, and 20% purple. The iso-activity wash between 30% and 100% changed from light blue to red.

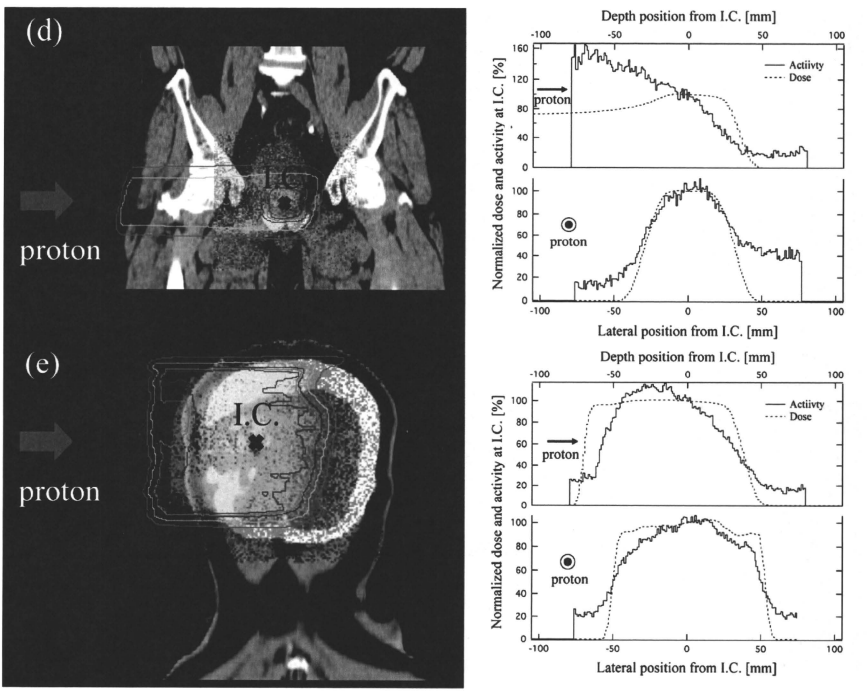

Fig. 4. (*continued*).

of the tumor's volume was more than 100 mL. Also, in carbon therapy, similar observation of the tumor shrinkage has been reported in (7). The BOLPs-RGp indicated that the proton irradiation dose was delivered to the brain stem of organs at risk.

Washout effect of the activity in the treatment period

A histopathologic examination demonstrated that higher activity was observed in regions containing necrotic liver cells than in any other region. The upper panel of Fig. 7 shows the calculated dose distribution and the measured activity distribution on a CT image taken at the first treatment of a 3.8 GyE delivery dose. The bottom left panel of Fig. 7 shows the number of detection counts per 20 s of activity in the regions of interest of areas A and B in the liver. Hence, the region of interest of area A is the necrotic region of the tumor, and area B is the normal tumor region. Therefore, area B-A is equivalent to the area of the tumor minus the necrotic region. The observed decay curves in the region of interest of area A and B-A were fitted well enough using a double exponential equation. The two half-lives of the double exponential fitting were 31 $\pm$ 8 s and 146 $\pm$ 20 s in the area A, and 21 $\pm$ 4 s and 164 $\pm$ 11 s in the area B-A, respectively. The half-life was longest in the necrotic region of the tumor. The activity images for the 200 s measurement by the BOLPs-RGp are shown in the left of Fig. 8. The high activity

Table 1. Summary of proton beam irradiation parameters

	Treatment site	Proton energy [MeV]	SOBP [mm]	Gantry angle [deg.]	Bed angle [deg.]	Fractional dose [GyE]	Irradiation time [sec.]
(a)	Head and Neck	123	90	0	0	2.5	39
(b)	Liver	137	70	270	0	3.8	229
(c)	Lungs	145	70	160	0	2.0	38
(d)	Prostate	187	50	270	0	2.0	15
(e)	Brain	122	90	330	90	2.5	40